Layer-By-Layer Printed Metal Hybrid (Cs:FA)PbI$_3$ Perovskite Nanocrystal Solar Cells

Manuel A. Reus, Ahmed Krifa, Quinten A. Akkerman, Alexander Biewald, Zehua Xu, David P. Kosbahn, Christian L. Weindl, Jochen Feldmann, Achim Hartschuh, and Peter Müller-Buschbaum*

Mixed halide perovskite nanocrystals in the form of cesium/formamidinium lead triiodide ((Cs:FA)PbI$_3$) offer great potential for efficient and stable solar cells. To date, large-scale production with roll-to-roll compatible deposition methods remains difficult and requires detailed research on each involved processing step. Here, a proof-of-concept study about slot-die coating (printing) the active layer of (Cs:FA)PbI$_3$-based nanocrystal solar cells is presented. Structural and morphological changes during ligand exchange of long-chain oleic acid and oleylamine by Pb(NO$_3$)$_2$, and top-layer FAI passivation are investigated. Ligand exchange improves the processability of the nanocrystal layer and enhances charge transport. It also changes texture from face-on toward edge-on orientation as grazing-incidence X-ray scattering studies indicate. Ligand exchange and FAI passivation redshift photoluminescence and prolong charge carrier lifetime in the printed nanocrystal films. The proof-of-concept feasibility of printing metal halide perovskite nanocrystal films for solar cells is shown by building 20 devices with a median power conversion efficiency of 6.39%.

M. A. Reus, A. Krifa, D. P. Kosbahn, C. L. Weindl, P. Müller-Buschbaum
Technical University of Munich, TUM School of Natural Sciences
Department of Physics
Chair for Functional Materials
James-Franck-Str. 1, 85748 Garching, Germany
E-mail: muellerb@ph.tum.de
Q. A. Akkerman, J. Feldmann
Chair for Photonics and Optoelectronics
Nano-Institute Munich, Department of Physics
Ludwig-Maximilians-University Munich
Königinstr. 10, 80539 Munich, Germany
A. Biewald, Z. Xu, A. Hartschuh
Department Chemie und CeNS
Ludwig-Maximilians-Universität München
Butenandtstr. 11, 81377 München, Germany
P. Müller-Buschbaum
Technical University of Munich
Heinz Maier-Leibnitz Zentrum (MLZ)
Lichtenbergstraße 1, 85748 Garching, Germany

1. Introduction

Metal halide perovskite quantum dots (PQDs) and perovskite nanocrystals (PNCs) are a remarkable extension to the existing manifold that constitutes the perovskite material class.[1,2] Perovskite materials are viewed as versatile semiconductors and light absorbers in LEDs,[3–6] photodetectors, thermoelectric, or photovoltaic devices with, for example, high absorption rates, long charge carrier diffusion lengths, and easy processability due to a high defect tolerance.[7–11] PQDs offer yet additional synthesis routes,[12] extended compositional stabilities,[13,14] and new processing opportunities with fresh optimization strategies.[2,15] For example, they offer greater stability for certain chemical compositions by ligand stabilization and show enhanced thin-film stability due to surface energy, lattice strain, and ligand shielding against, for example, moisture.[5,15] By controlling the size and shape, the band gap energy and optical absorption can be highly tuned, which is not as easy for the corresponding bulk materials.[13,16,17] Ligand chemistry is another key aspect of quantum dots (QDs). Usually, QDs contain amphiphilic ligands attached to the surface; thus, stabilizing the surface and keeping QDs in solution. The surface chemistry is heavily impacted by ligand choice and offers great tuning potential for stabilization, functionalization, and processing.[18] For example, Wheeler et al. showed that a targeted ligand exchange can improve the electronic coupling between QDs.[19] Oleic acid (OA) and oleylamine (OAM) are standard long-chain ligands for PQDs, but charge transport and stabilization can be improved by adding short-chain ligands such as octanoic acid or octylamine.[20]

As perovskite solar cells reach power conversion efficiency (PCE) values above 25% and perovskite modules surpass 20% PCE,[21,22] Park et al. identified five categories that need to be addressed in the coming decade: pushing the PCE toward the theoretical limit, improving large-area coating strategies, increasing the long-term stability, integrating recycling strategies, and applying PQDs to tandem devices.[23] Scalable deposition techniques offer the potential for fast and cheap production, especially when combined with scaled PQD synthesis.[24,25] All-printed perovskite bulk solar cells reach over 10% PCE, as reported by Beynon et al. in 2023.[26] A recent techno–economic study identifies synthesis

**ADVANCED
SCIENCE NEWS**

www.advancedsciencenews.com

**ADVANCED
OPTICAL
MATERIALS**

www.advopticalmat.de

scaling, solvent recycling, and process automation as crucial factors for cost reduction.[27] Multiple deposition methods are capable of large-area coating, for example, spray coating,[28] blade coating, slot-die coating,[29] or inkjet printing.[15,30] A decisive advantage in QD deposition is that the crystallization process is decoupled from the deposition in contrast to popular solution-based bulk synthesis.[31] Thus, crystallization and deposition can be tailored and controlled separately.[25,27,30] This approach can be of great importance for device fabrication and has been shown to lead to exceptional results in PQD-based solar cells, with PCEs reaching 16.6% for mixed (Cs:FA)PbI$_3$ systems.[32] Specialized surface passivation by Cs$^+$ in CsPbI$_3$ PQD solar cells led to PCEs around 14%,[33] and Fangchao et al. reached 15.6%[34] in mixed CsPbI$_3$/FAPbI$_3$ PQD photovoltaic devices. In 2020, PQD solar cells with 18.1% PCE were reported by UNIST.[35]

However, these results were obtained with spin coated devices; and are therefore, of limited use for large-area coating approaches due to high material loss, non-continuous production, and limited large-area coating capabilities. Presently, not much is known about the device performance and the influence on structure and morphology when using scalable PQD deposition methods, and a very limited number of publications deal with the printing of PQDs. Sorrentino et al. reached 3.7% for CsPbBr$_3$ nanocrystal solar cells,[36] but even recent studies and reviews do not mention printed PQD or PNC solar cells or focus solely on printed PbS systems.[37–40]

Here, we investigate morphological, structural, and optoelectronic changes that printed thin film perovskite nanocrystal (PNC) layers undergo during the multiple processing steps required for PV devices. With respect to real-word application, printing in ambient conditions is highly desirable because inert conditions will add extra costs and challenges. Consequently, the aim of the current study was to establish a scalable fabrication route that works in air and is focused on simplicity and material efficiency. We give insights into textural changes by grazing-incidence wide-angle X-ray scattering (GIWAXS) because orientation can influence the charge transport properties as shown by recent studies about facet-dependent transport properties.[41–43] We also investigate optoelectronic changes by fluorescent lifetime imaging (FLIM) and couple the results with surface topography. Finally, we present printed layer-by-layer deposited PNC thin-film solar cells with a median PCE of 6.39%. To the best of our knowledge, perovskite solar cells with a slot-die coated active layer of colloidal (Cs:FA)PbI$_3$ nanocrystals have not been reported before. In this work, we focus on the translation of active layer deposition to slot-die coating.

Solar cell focused publications tend to use the term "quantum dot" that originates from PbS-based quantum dot solar cells.[44] However, it is sometimes used for sizes above 10 nm where only limited quantum confinement effects are present.[11,32] For larger particle sizes, the term "nanocrystals" appears more appropriate;[25,45] and therefore, is used in this work.
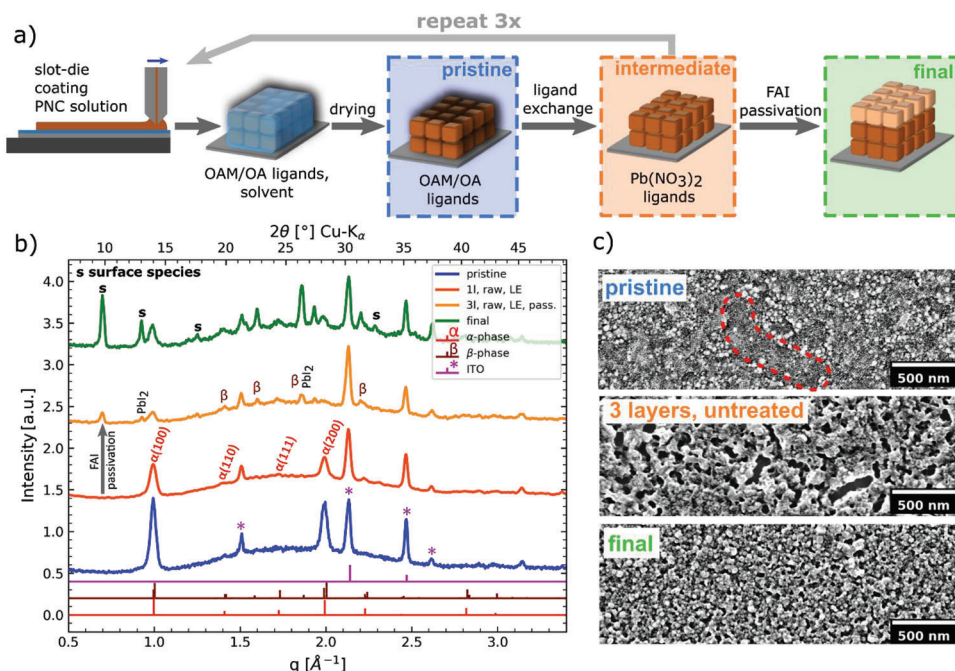
2. Results and Discussion

Building up PNC layers for solar cells is challenging for multiple reasons. Reaching layer thicknesses that allow for sufficient light absorption is not easy with PNC ink concentrations being limited. Highly concentrated PNC inks are less stable and need to be processed quickly. As described above, a layer-by-layer deposition is traditionally used, which means repeating the deposition step sequentially multiple times. However, the layer quality must remain high, and damage by post-processing and the subsequent layer deposition must be minimal. In this work, we apply the deposition strategy of sequential layer-by-layer deposition to meniscus-guided slot-die coating of (Cs:FA)PbI$_3$ (cesium formamidinium lead iodide) NC ink in ambient conditions. We use a hot injection ternary route for the PNC synthesis reported before by Akkermann et al.[12] A schematic overview of the layer deposition and the post-treatment is shown in **Figure 1**a. Layer-by-layer slot-die coating deposition is done in air and the substrate is heated to 30 °C to avoid fluctuating results depending on the room temperature. We print octane-based PNC ink (70 mg mL) at a speed of 10 mm s^{-1} with a gap height of 200 µm onto glass/ITO/SnO$_2$ (indium tin oxide and tin oxide) substrates. The print speed falls into the Landau–Levich regime and is comparable with previous reports on scalable device fabrication.[46,47] If ink/print parameters for higher print speeds can be found, a higher layer thickness is to be expected.[48] After deposition, we let the solvent evaporate at 30 °C for 1 min and continue with the ligand exchange step to enable better interparticle and inter-layer charge transport. This is done by partially replacing OA (oleic acid) and OAM (oleylamine) ligands with smaller Pb(NO$_3$)$_2$ (lead nitrate). Samples are washed with Pb(NO$_3$)$_2$-saturated MeOAc (methyl acetate) solution and then rinsed with neat MeOAc. The excess solution is removed by spin coating. Printing and ligand exchange is repeated three times to reach the desired film thickness of more than 100 nm. The final PNC layer is passivated with a saturated FAI (formamidinium iodide) in EtOAc (ethyl acetate) solution and rinsed with neat MeOAc. Spin coated spiro-OMeTAD (2,2′,7,7′-tetrakis[N,N-di(4-methoxyphenyl)amino]–9,9′-spirobifluorene) acts as electron blocking layer. Last, a gold layer is evaporated onto the layer stack; thus, finishing the last layer of the n–i–p solar cell device. A detailed experimental description is provided in the Experimental Section.

In this work, we compare two distinct thin films on the route toward fabricating printed PNC solar cells to gain insights into the changes that occur during pre- and post-processing. The two films are labeled 'pristine' and 'final' and are marked with blue and green boxes in Figure 1a, respectively. For the pristine printed layer, no pre-deposition of the ink purification is done, and no post-deposition ligand exchange or FAI passivation is done. For the final thin film, which is used for building solar cells, the PNC ink is purified before deposition, and the film consists of three layers, ligand exchange is applied, and the final layer is passivated with FAI. We complement our findings with additional measurements of intermediate processing steps, which are marked in orange in Figure 1a. The experimental details about the intermediate steps are given with each measurement.

We begin by investigating the crystal structure with X-ray diffraction (XRD). Figure 1b shows XRD data normalized to the highest peak intensity. The pristine (Cs:FA)PbI$_3$ thin film shows a cubic structure. Simulations using VESTA for the cubic α-phase (Pm-3m, a = 6.313 Å), the tetragonal β-phase (P4/mbm, a = 8.876 Å, b = 6.324 Å), and SnO$_2$/ITO are shown for comparison.[13,49] For the pristine film, only α-perovskite and

ADVANCED
SCIENCE NEWS

www.advancedsciencenews.com

ADVANCED
OPTICAL
MATERIALS

www.advopticalmat.de

Figure 1. a) Deposition process for $(Cs:FA)PbI_3$ thin films from colloidal nanocrystal ink. b) XRD data of printed perovskite thin films from PNC ink. XRD data is shown for a pristine layer (blue), one layer from raw ink with ligand exchange (LE, red), one layer from raw ink with ligand exchange and FAI passivation (orange), and the final thin film consisting of three layers from purified ink with ligand exchange and FAI passivation (green). c) SEM images of a pristine layer (area of high order marked in red), three layers deposited from raw ink and no post-deposition treatment, and the final film.

ITO/SnO_2 can be identified and are indexed in red and purple, respectively. This is in accordance with literature.[12,13] The successful synthesis is further confirmed by UV–vis measurements shown in Figure S3, Supporting Information. XRD studies in air and ambient conditions show the stability of the printed PNC layers (cf. Figure S4, Supporting Information). The red curve in Figure 1b shows a film after $Pb(NO_3)_2$ ligand exchange, which does not influence the crystal structure. However, FAI passivation leads to the introduction of the β-phase. As previously reported, a loss or a reduction of surface ligands can induce phase conversions via surface defects.[20] After FAI passivation, traces of PbI_2 can be identified, which hints toward a partial decomposition. In addition, FAI treatment leads to excess FAI on the PNC surface. This observation is apparent from scanning electron microscopy (SEM, Figure S9, Supporting Information) and is confirmed by XRD measurements that display Bragg peaks that are also observed for drop cast FAI from EtOAc (see Figure S6, Supporting Information). A new peak at $q = 0.698$ Å^{-1} ($2\theta = 9.82°$) appears only after FAI passivation, corresponding to a d-spacing of 9.00 Å. It does not originate from pure FAI, which shows different Bragg peak positions (see Figure S6b, Supporting Information). As treatment with pure EtOAc does not induce any changes visible in the XRD studies (see Figure S6a, Supporting Information), it is suggested that FAI intercalates into the PNC layer, thereby changing the lattice spacing of the perovskite crystal structure. It was shown by Wheeler et al. that ligands can influence PNC spacing.[19] At this point, the detailed mechanism of octane-assisted FAI intercalation is not clear and further studies need to be conducted. We encourage researchers to show low-angle XRD data more frequently, that is, below $2\theta = 10°$.

SEM images reveal apparent differences between the pristine and final films (Figure 1c). The pristine film has full coverage and shows regions of high order (marked in red). This high order is also present for pure $CsPbI_3$ and $FAPbI_3$ NC films shown in the Supporting Information (Figure S1, Supporting Information). TEM images confirm the cubic shape of the PNCs and an edge length of $\approx$12–15 nm (Figure S2, Supporting Information). The final film shows less order but exhibits a good homogeneity while keeping the nanocrystalline surface characteristics. Some fusion of PNCs into bigger aggregates is observed (sintering). However, without surface treatment, three sequential printing steps of purified ink lead to pinholes and a rough and inhomogeneous surface. We conclude that post-deposition ligand exchange protects the NCs against re-dispersion into the ink when printing the subsequent layer. Increasing the resistivity against the ink solvent by increasing compactness and reducing hydrophobicity of the ligand shell proves crucial for layer-by-layer printing. A picture of the printing process under UV light is shown in Figure S7, Supporting Information.

PNC sintering and surface morphology changes are suspected to impact optical properties, which we probe with fluorescent lifetime imaging (FLIM). An area of 20×20 µm^2 is investigated for the pristine and final film. The normalized PL intensity, central energy, and a short and a long lifetime are shown in **Figure 2**a,b. Experimental and fit details can be found in the Experimental Section. The pristine layer shows a homogeneous surface characteristic (Figure 2a). The average PL emission peak is shown in Figure 2c, and two centers around 1.69 eV ($\pm$0.02%) and 1.75 eV ($\pm$0.05%) are identified, which is attributed to two different size distributions of NCs in the unpurified ink. The average lifetimes
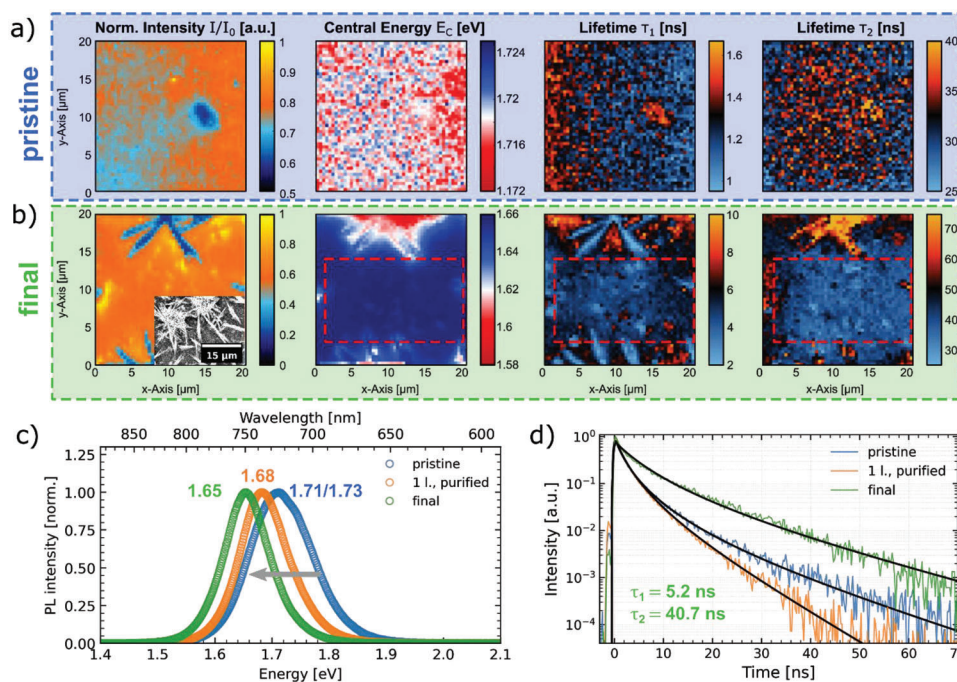
Figure 2. a) FLIM data for one printed layer on glass/ITO/SnO$_2$ from raw (Cs:FA)PbI$_3$ NC ink (pristine, blue) and b) three layers printed from purified NC ink with subsequent ligand exchange and FAI passivation (final, green). For each dataset spatially resolved normalized PL intensity I, central PL energy E_c, short lifetime τ_1 and long lifetime τ_2 are shown (from left to right). c) Average PL data from a 20 × 20 μm^2 area and d) average transient PL data extracted from FLIM measurements of the respective printed thin films. For (c,d), additional data for one layer printed from purified ink is shown (orange).

τ_1 and τ_2 are (1.3 ± 0.2) ns and (32.1 ± 2.6) ns and lie in the range reported by other publications.[4,50,51] A thin film printed from purified PNC ink exhibits only a single emission center located at around 1.68 eV (±0.01%), which shows the successful homogenization of the NC size distribution. The lifetimes decrease to (1.3 ± 0.1) ns and (13.7 ± 2.2) ns. It is speculated that the purification process, which includes the removal of excess ligands, destabilizes the NCs and deteriorates their optical properties.[20] This assumption is in accordance with the XRD data shown in Figure S5, Supporting Information, where a clear appearance of the β-phase is observed after FAI passivation. In Figure S10, Supporting Information, the PL emission map indicates a redshift in some spots, which is attributed to PNC agglomerates. In the final film, the average PL emission center is at 1.65 eV (±0.01%), τ_1 = (5.2 ± 0.8) ns, and τ_2 = (40.7±5.4) ns (Figure 2c,d). Again, the redshift is attributed to the exchange of the long-chain ligands OA and OAM before the subsequent layer is deposited, which leads to the sintering of the PNCs (fusion of multiple NCs to form a bulk-like film morphology). Parts of the surface are covered with the needle-shaped surface species, identified before as FAI (Figure S9, Supporting Information). These areas show a redshifted PL emission and decreased τ_1 and increased τ_2. A PL redshift after FAI passivation has been reported before.[19] Within the red box (Figure 2b), the surface is homogeneous, the PL emission center is at (1.66 ± 0.01) eV, τ_1 = (4.06 ± 0.86) ns, and τ_2= (42.8 ± 5.9) ns. The influence of the needle-shaped FAI surface features appears to be rather small because the average transient PL curve is clearly decaying slower than for the pristine and intermediate films (Figure 2d). It can be concluded that the FAI pas-

sivation positively prolongs the charge carrier lifetime in printed PNC layers.

Pre- and post-deposition treatment of the NCs commonly influence the morphology and optical properties of the thin film. We suspect this implies orientational changes in the PNCs. Therefore, we perform grazing-incidence wide- and small-angle scattering (GIWAXS and GISAXS) on pristine, final, and intermediate printed PNC films. Experimental details and information on the post-processing of GIWAXS and GISAXS images are given in the Experimental Section. In **Figure 3**a–c, GIWAXS data is shown of the pristine film, the intermediate film consisting of three layers (printed from raw ink, with ligand-exchange treatment, no FAI passivation), and the final film. Full GIWAXS and GISAXS detector images can be found in Figure S8, Supporting Information. XRD studies suggest a cubic α-perovskite phase and Bragg ring locations fit well; for example, we identify the (100) and (200) at 1.0 and 2.0 Å^{-1}. However, the predominant PNC orientation is different for the three films, as can be clearly seen when comparing Figure 3a–c. To visualize the changes, in Figure 3d, azimuthal tube cuts of the (100) Bragg reflex are shown. The pristine film shows a high degree of order with a FWHM of 18° located around 0° and 90°. The GIWAXS data can be indexed for a (001) Bragg plane parallel to the substrate; in short, we write (001)$_{\parallel S}$. This orientation is also illustrated in Figure 3e, with unit cells of the α-perovskite phase depicted for different orientations. A ligand exchange with Pb(NO$_3$)$_2$ leads to a predominantly (111)$_{\parallel S}$ orientation (Figure 3b). Moreover, the distribution is significantly broadened to 36°FWHM, demonstrating a loss of long-range order. The ligand exchange
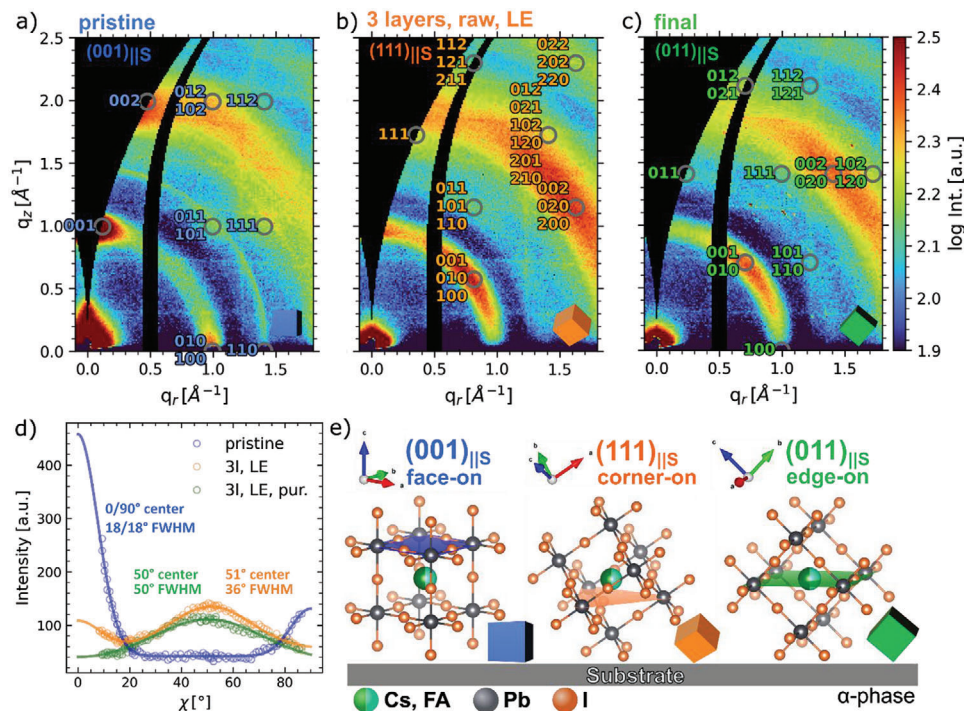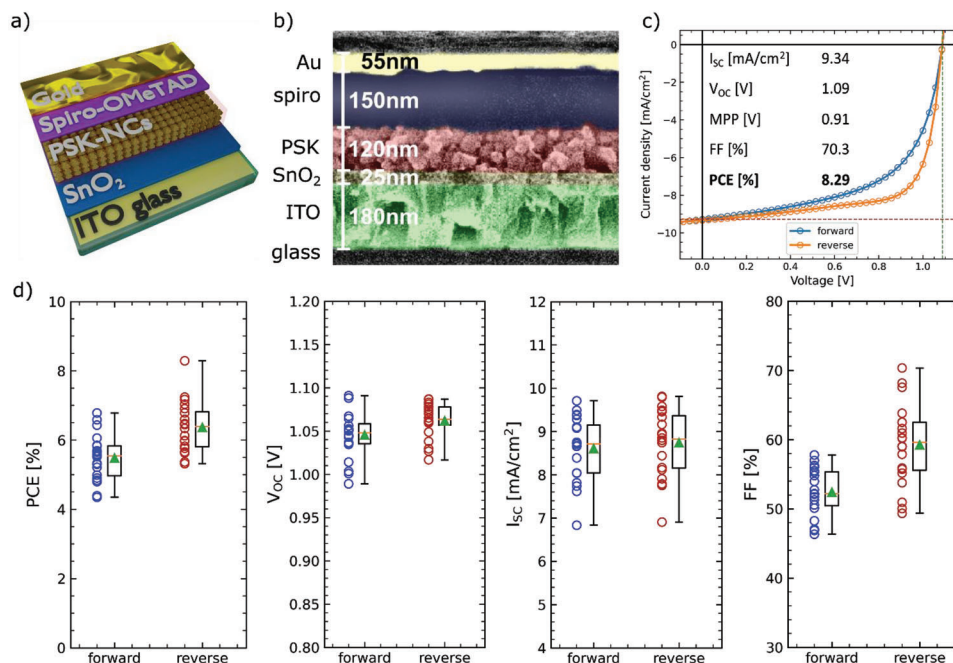
Figure 3. 2D GIWAXS data of a) a pristine layer, b) a layer deposited from purified ink and after the ligand exchange process, and c) a thin film consisting of three printed layers from purified PNC ink and after the ligand exchange process. Bragg spots are indexed using the perovskite α-phase, and the respective orientation is given with respect to the substrate plane. d) Azimuthal tube cuts of the 2D GIWAXS data of the (001) Bragg reflex of the (Cs:FA)PbI$_3$ perovskite thin film. e) Illustrations of crystallite $(001)_{\parallel S}$, $(111)_{\parallel S}$, and $(011)_{\parallel S}$ orientations with respect to the substrate.

influences the stacking behavior of the PNCs and pushes them toward the corner-on $(111)_{\parallel S}$ orientation. Some remaining face-on $(001)_{\parallel S}$ orientation can be identified. This finding is attributed to the two identified size distributions (see PL measurements and Figure 2), where the larger PNCs are still present and more reluctant to arrange themselves in an edge-on orientation. In general, NC stacking is driven by minimizing the surface area to minimize surface energy and by maximizing the system's entropy.[52,53] The surface energy of the bottom layer influences the wetting behavior of the subsequent ink deposition.[54–56]

In the final film after purification, a weakening of the face-on orientation continues. Here, we see a slightly changed orientation toward the $(011)_{\parallel S}$ edge-on orientation, which resembles a slight rotation away from the substrate, lifting up one end of the PNC edge. This behavior is illustrated in Figure 3e (green). The order of the PNCs decreases with the ligand exchange and the FAI passivation; in the final film, the (001)-Bragg peak shows a FWHM of 50° centered at $\chi = 50°$. In conclusion, GIWAXS studies reveal a trend toward the edge-on orientation if short-chain ligands are used. A preferential orientation for PNCs was also reported by Li et al., however, the order was far less pronounced, and so far, it is unclear if strong order is beneficial for charge transport in PNC layers.[34] Furthermore, the thicker (multilayer) film seems to prefer the corner-on/edge-on orientation (cf. Figure 3b,c). This leads to the speculation that the SnO$_2$-perovskite/ligand interface promotes a different texture than the perovskite nanocrystals surrounded by other nanocrystals/ligands. It could be similar to a templating effect reported before by W. Chen et al.[57]

The order of the PNCs is also visible in the GISAXS measurements (Figure S11, Supporting Information). Horizontal line cuts are performed around the Yoneda region of the perovskite (exit angle α_f between 0.1869° and 0.2291°, vertical width ≈6 pixels). Cuts are shown in Figure S12, Supporting Information for ITO on glass, pristine, intermediate, and final NC films. The horizontal line cut of the pristine NC film shows a distinct peak at around 0.3 nm^{-1}. The curve can be modeled (for details, see Experimental Section) with three structures and the result is shown in Figure S13, Supporting Information. The model suggests NCs with a radius of ≈5.3 nm, which is in good agreement with SEM and TEM imaging. The interdot distance is around 13.4 nm. The ligand shell overlaps with a radius of 1.4 nm and leads to scattered intensity in the high q-region around 0.5–1.1 nm^{-1}. A schematic model of the PNC arrangement is shown in Figure S13, Supporting Information. However, the order is lost in the intermediate and final films, as is apparent by the disappearance of the peak around 0.3 nm^{-1} in Figure S12, Supporting Information. In combination with findings from GIWAXS tube cuts where the FWHM of the orientation distribution increases from 18° to 50° for the final film (Figure 3d), a decrease in preferred orientation and a decrease in long-range order can be concluded.

To demonstrate the feasibility of slot-die coated PNC solar cells, as a proof-of-concept, we build solar cell devices. In **Figure 4**a, the layer stack of our n–i–p device architecture of the solar cells is shown, which is built up of glass/ITO/SnO$_2$/(Cs:FA)PbI$_3$ PNCs/spiro-OMeTAD/Au. A SEM cross-section (Figure 4b) reveals an active layer thickness of ≈120 nm. The active layer is made of three printed PNC layers (photograph in

**ADVANCED
SCIENCE NEWS**

www.advancedsciencenews.com

**ADVANCED
OPTICAL
MATERIALS**

www.advopticalmat.de

Figure 4. a) Scheme of the layer stack used for the n–i–p device architecture of the printed solar cells based on $(Cs:FA)PbI_3$ colloidal NC ink. b) Cross-sectional SEM image of the PNC solar cell layer stack. c) Best IV curve of PNC solar cells fabricated from $(Cs:FA)PbI_3$ colloidal NC ink. d) Extracted solar cell parameters (power conversion efficiency PCE, open circuit voltage V_{OC}, short circuit current I_{SC}, and fill factor FF) of 20 fabricated solar cells. The median (orange line) and the average (green triangle) are shown for each solar cell parameter. 50% of the data lies within the range of the box. The whiskers show the complete data range.

Figure S14, Supporting Information) and combined into a solar cell (photograph in Figure S7, Supporting Information). 20 solar cells are produced for reliable statistics and current–voltage measurements (IV) are performed after 1 week. They reveal a reverse scan median PCE value of 6.39%, a median open circuit voltage (V_{OC}) of 1.06 V, a median short circuit current (I_{SC}) of 8.82 mA cm^{-2}, and a median fill factor (FF) of 59.61%. The IV parameter distribution is shown in Figure 4d. An IV curve of a PNC solar cell with an efficiency around the median value is shown in Figure S15, Supporting Information. The IV curve of the best obtained solar cell is shown in Figure 4c with a PCE of 8.29% (I_{SC} = 9.34 mA cm^{-2}, V_{OC} = 1.09 V, FF = 70.3%). To the best of our knowledge, no previous reports on slot-die coated $(Cs:FA)PbI_3$ PNC solar cells exist today. Compared to the current state-of-the-art spin coated $(Cs:FA)PbI_3$ PNC solar cell with a PCE of 16.6%,[32] our printed solar cells mainly lack high short circuit currents, whereas V_{OC} and FF deviate no more than 10% from the spin coated counterparts. A logical next step in further research projects will be the development of (mini-)modules, which require even wider slot-die heads and suitable solar cell fabrication equipment. The rather small current is attributed to the quite thin PNC layer of only 120 nm in the present study. Higher film thicknesses of equal quality are not easily obtained by simply repeating more printing deposition steps. We observe that delamination is more likely to occur with increasing layer number, potentially indicating an insufficiently strong layer interconnection. Increasing drying times and introducing low-temperature annealing times might prove beneficial, but further experiments are needed for conclusive data interpretation. Increasing the PNC concentration might also be beneficial; however, this can drasti-

cally reduce the shelf lifetime of the PNC ink. Further optimization and process engineering will be required to enable thicker printed active PNC layers.

To investigate the influence of processing on solar cell performance, devices with raw and purified NC ink, with and without ligand exchange, and one or three layers are fabricated. IV data is shown in Figure S16, Supporting Information. It is apparent that multiple layers of PNCs increase the I_{SC} and lead to an increase in V_{OC}. This finding is due to the increased absorber layer thickness, which allows more photons to be absorbed. $Pb(NO_3)_2$ ligand exchange also improves the I_{SC}, which is attributed to a better inter-PNC charge transport. Interestingly, for further efforts to increase the thickness of the absorber layer, we observe that ligand exchange is necessary for building up multiple layers. It decreases the likelihood that the NC layer is damaged by the subsequent layer in the layer-by-layer deposition process. The ligand exchange seems to lead to a higher resistance against the solvent contained in the ink, possibly due to higher layer density and less hydrophobic chain ends that interact with the hydrophobic solvent octane.

3. Conclusion

In conclusion, we present a proof-of-concept layer-by-layer deposition method for slot-die coated $(Cs:FA)PbI_3$ perovskite nanocrystal solar cells with a median PCE of 6.39 %. $Pb(NO_3)_2$ ligand exchange and multilayer deposition induce structural changes from purely cubic toward a mixture of α- and β-phase. A PL redshift from 1.69 to 1.65 eV hints toward the sintering of the PNCs during the ligand exchange. The perovskite orientation

with respect to the substrate depends on the processing parameters. We find that ligand exchange, purification, and surface passivation with FAI influence the orientation of the PNCs. Pristine layers are highly ordered in face-on orientation, but rearrangement toward an edge-on dominated texture occurs upon multilayer processing. We conclude that working solar cells can be readily obtained from printed (Cs:FA)PbI$_3$ PNCs and the development of PNC (mini-)modules holds promise for a successful implementation. Still, processing plays a vital role in NC orientation, morphology, PL emission center, and charge carrier lifetime, which influence solar cell parameters. Further research is needed for fully scalable and economically viable PNC solar cell production, making each layer and processing step scalable and sustainable. We hope our findings will inspire further research of printed PNC solar cells and help research toward scalable production of PNC devices.

4. Experimental Section

Perovskite Nanocrystal Synthesis: The synthesis of (Cs:FA)PbI$_3$ perovskite nanocrystals was based on a recipe reported by Akkerman et al.[12] Oleylamine iodide (OLAM-I) was synthesized from iodine (I$_2$, 1.5 g, Sigma–Aldrich, 99.8%) and oleylamine (OAM, 9 mL, Sigma–Aldrich) and stirred at 200 °C in 1-octadecene (ODE, 21 mL, Sigma–Aldrich, 90 %).

FAPbI$_3$ NCs were synthesized by mixing formamidinium acetate (FAOAc, 250 mg, Sigma–Aldrich, 99%), lead acetate (PbOAc$_2$·3H$_2$O, 303 mg, Sigma–Aldrich, 99.99 %), oleic acid (OA, 0.8 mL, Sigma–Aldrich, 90%), and octadecene (20 mL) in a flask. The mixture was heated to 80 °C under constant stirring. After the solution became clear, OLAM-I (6 mL) was added rapidly, and the solution was cooled quickly in an ice bath. CsPbI$_3$ NCs were synthesized by mixing cesium carbonate (Cs$_2$CO$_3$, 65 mg, Sigma–Aldrich, 99 %), lead acetate (303 mg), oleic acid (0.8 mL), and octadecene (20 mL) in a flask. The mixture was heated to 165 °C under constant stirring. Then, OLAM-I (8 mL) was added rapidly, and the solution was cooled quickly in an ice bath. FAPbI$_3$ and CsPbI$_3$ NC crude solutions were purified by centrifugation at 8000 rpm for 15 min and the supernatant was discarded. The dry NCs were weighed and then redispersed in octane (Sigma–Aldrich, 99%, anhydrous) and mixed in the ratio 0.46:0.54 CsPbI$_3$:FAPbI$_3$ to yield 4–5 mL (Cs:FA)PbI$_3$ ink at a concentration of 70 mg mL^{-1} with an estimated 1:1 molar ratio of Cs:FA.

NC Deposition Via Slot-Die Coating: (Cs:FA)PbI$_3$ ink (70 mg L^{-1} in octane) was deposited using a custom-built modular slot-die coater. The gap height was 200 µm, the print speed 10 mm s^{-1}, the substrate temperature 30 °C, and the pumping speed 150 µL min^{-1}. All samples were printed in ambient air with a rel. humidity below 50 %. The slot-die width was 25 mm. 60 s of waiting time was added to let the solvent evaporate before the ligand-exchange process. The ligand-exchange was done by applying three solutions sequentially: a saturated lead nitrate (Pb(NO$_3$)$_2$, Sigma–Aldrich, 99.999%, 20 mg) solution in MeOAc (20 mL), a saturated formamidinium iodide (FAI, Sigma–Aldrich, 98%, 20 mg) solution in EtOAc (30 mL), and a neat MeOAc solution. The FAI and lead nitrate solutions were prepared by mixing the specified amounts and sonicating for 10 min. The excess salt was removed by centrifuging at 3500 rpm for 5 min. The Pb(NO$_3$)$_2$ solution (≈350 µL) was carefully dropped onto the substrate and removed by spin coating for 10 s at a speed of 1000 rpm and a ramp of 2 s, followed by 20 s at a speed of 2000 rpm and a ramp of 3 s. This step was followed by spin coating with neat MeOAc (≈350 µL, for 10 s, 1000 rpm, 2 s ramp; followed by 20 s, 2000 rpm, 3 s ramp). These steps were repeated to build up multiple layers. The final PNC layer was passivated with FAI: saturated FAI solution was distributed onto the substrate (≈350 µL, 10 s waiting time) and removed by spin coating (10 s, 1000 rpm, 2 s ramp; followed by 20 s, 2000 rpm, 3 s ramp). The layer was cleaned with neat MeOAc which was removed by spin coating (≈350 µL, 10 s waiting time, 10 s, 1000 rpm, 2 s ramp; followed by 20 s, 2000 rpm, 3 s ramp).

For some samples, the NC ink was purified shortly before deposition, which is mentioned in the text accordingly. For this step, ethyl acetate was added in a ratio of 2:1 and the mixture was centrifuged for 5 min at 8000 rpm at room temperature. The supernatant was discarded and the original volume of octane was added to redisperse the NCs. If no purification step was done, the NC ink was named "raw."

Solar Cell Fabrication: For solar cell production, a glass substrate with pre-patterned indium tin oxide (ITO, Yingkou Shangneng Photoelectric Material Co. Ltd., 15 Ω □$^{-1}$ sheet resistance, 25 × 75 mm^2 area, 1.1 mm thickness) was used. Substrates were cleaned in a sonicater for 10 min each in water-based Hellmanex III solution (Hellma), DI water, acetone, ethanol, and isopropanol and then dried under a stream of nitrogen. For the hole blocking layer, tin oxide (SnO$_2$, Alfa Aesar, 15% colloidal dispersion in water) was diluted in DI water with a ratio of 1:4. The solution was shaken at room temperature for 30 min; and then, spin coated for 30 s with 4000 rpm and a ramp of 6 s on a UV/ozone plasma cleaned ITO substrate. The layer was annealed for 30 min at 150 °C. The perovskite layer was deposited by slot-die coating as explained above in the section NC Deposition Via Slot-Die Coating. As electron blocking layer spiro-OMeTAD (2,2′,7,7′-tetrakis[N,N-di(4-methoxyphenyl)amino]−9,9′-spirobifluorene) was used. In a nitrogen-filled glovebox, a LiTFSI solution consisting of LiTFSI (520 mg, Sigma–Aldrich, 99.95%) and acetonitrile (1 mL, Sigma–Aldrich, 99.8%, anhydrous) and a FK209 solution consisting of FK209 (358 mg, Tris(2-(1H-pyrazol-1-yl)−4-tert-butylpyridine)cobalt(III) tri[bis-(trifluoromethane)sulfonimide], Dyesol) in acetonitrile (1 mL) were prepared. For the final spiro-OMeTAD solution, 73.5 mg spiro-OMeTAD (Sigma–Aldrich, 99%), 1 mL chlorobenzene, 28.8 µL tBP (4-tert-butylpyridine, Sigma–Aldrich, 98%), 17.5 µL LiTFSI solution, and 4 µL FK209 solution were mixed. The solution was dynamically spin coated onto the perovskite for 10 s (4000 rpm, 4 s ramp). The top Au electrode was evaporated at 10^{-6} mbar at ≈0.2 nm s^{-1} until the final thickness of ≈80 nm was reached.

Solar Cell Characterization: An LS0500 (LOT Quantum Design) with a xenon lamp was used for current–voltage (IV) characterization. The spectrum was close to an AM1.5G spectrum with the intensity of "one sun" which is 100 mW cm^{-2}. The lamp intensity was calibrated with a KG5 filtered reference Si-based solar cell (Fraunhofer ISE certified). The illuminated area was defined by a metal sheet mask with an opening of 0.1 mm^2 and IV measurements were recorded at room temperature in ambient air with a Keithley 2611B source meter (Tektronix).

XRD: A D8 Advance X-ray diffractometer (Bruker AXS) with Göbel-mirror filtered Cu K$_{\alpha 1}$-radiation (λ = 1.5406 Å) was used for X-ray diffraction. Measurements were performed between 5 and 50 2θ with a step size of 0.03 2θ and an integration time per step of 2 s.

SEM: A Zeiss Gemini NVision 40 FIB-SEM (Carl Zeiss AG) was used for surface and cross-sectional scanning electron microscopy imaging. The beam energy was 5 keV and the working distance 3–5 mm. A Python script was used to adjust brightness and contrast for better visibility of single particles.

GIWAXS/GISAXS: Grazing-incidence wide- and small-angle X-ray scattering was performed on a Ganesha scattering device (Saxslab/Xenocs) with a GeniX3D X-ray source (λ = 1.5406 Å) and a Pilatus 300k detector (Dectris Ltd., pixel size 172 × 172 µm^2). For GIWAXS/GISAXS, a sample-to-detector distance of 95.6/1045 mm and an incidence angle of 0.375°/0.4° was used, respectively. The software package INSIGHT was used for data treatment and performing azimuthal tube cuts and horizontal cuts at the Yoneda region for GISAXS modeling.[58] Image intensity was corrected for solid angle, detector pixel sensitivity, and air attenuation using absorption coefficients for Si and air of 2.33 mm^{-1} and 1.1839 × 10^{-3} mm^{-1}. GISAXS modeling was performed using the local mono-disperse approximation (LMA) together with the distorted wave Born approximation (DWBA), as was done previously.[59–61] Thus, the scattering intensity could be expressed as $I(\vec{q}) \propto \sum_i N_i \langle |F(\vec{q}, R_i)|^2 \rangle S(\vec{q}, R_i)$, with the number of scatterers N, the form factor F, the structure factor S, and the momentum transfer q and radius R. Here, three decoupled cylindrical form factors were used in a 1D paracrystalline structure, using the effective interface approximation.[62]

FLIM: For fluorescent lifetime imaging consisting of photoluminescence (PL) measurements, hyperspectral images, and time resolved PL images, a custom-built confocal laser scanning microscope was used. It was based on a microscope body (Nikon), which was combined with an xyz-piezo-scanning stage (Physik Instrumente). The samples were measured upside down in epi-direction with an air objective (0.85 NA, Nikon). A beam splitter (Melles Griot 03BTL005) and a spectral 490 nm long pass filter were used to separate the laser from the PL light. A sub-picosecond laser (ichrome Toptica), which is tunable from 476 to 645 nm, was used for excitation. Here, 476 nm laser light was used, which was additionally filtered by a bandpass 473/10 nm (Chroma) in the excitation arm. The detection side consisted of two parts, which were separated by a flip-able mirror. One had an avalanche photodiode (APD, type: MPD PDM, detector size 50×50 μm^2), which was combined with a Time-Correlated Single Photon Counting (TCSPC) electronics (Becker und Hickel) measuring time-resolved PL transients. The second part consisted of a spectrometer (Andor Shamrock SRi303) combined with an open electrode CCD camera (Andor Newton DU920) for detecting spectra. The data were recorded using a customized Labview (Nation Instruments) program that combined the manufacturers' software with the authors' desired measurements. Further processing and analysis were carried out using a Matlab (Mathworks) program to obtain the PL spectra, TCSPC transients, and images. An antisymmetric fitting function was used to model the PL data.[63,64]

TEM: Transmission electron microscopy (TEM) images were acquired on a JEOL JEM-1011 operating at 80 keV. TEM samples were prepared by drop casting diluted NC solutions onto copper TEM grids.

Absorption Spectroscopy: Absorption spectra were recorded with a Cary 60 UV–vis spectrophotometer (Agilent Technologies).

Supporting Information

Supporting Information is available from the Wiley Online Library or from the author.

Conflict of Interest

The authors declare no conflict of interest.

Data Availability Statement

The data that support the findings of this study are available from the corresponding author upon reasonable request.

Keywords

GIWAXS, nanocrystals, perovskites, printing, slot-die coating, solar cells

[1] Q. A. Akkerman, G. Raino, M. V. Kovalenko, L. Manna, *Nat. Mater.* **2018**, *17*, 394.

[2] A. Dey, J. Ye, A. De, E. Debroye, S. K. Ha, E. Bladt, A. S. Kshirsagar, Z. Wang, J. Yin, Y. Wang, L. N. Quan, F. Yan, M. Gao, X. Li, J. Shamsi, T. Debnath, M. Cao, M. A. Scheel, S. Kumar, J. A. Steele, M. Gerhard, L. Chouhan, K. Xu, X. G. Wu, Y. Li, Y. Zhang, A. Dutta, C. Han, I. Vincon, A. L. Rogach, *ACS Nano* **2021**, *15*, 10775.

[3] Y.-H. Kim, S. Kim, A. Kakekhani, J. Park, J. Park, Y.-H. Lee, H. Xu, S. Nagane, R. B. Wexler, D.-H. Kim, S. H. Jo, L. Martínez-Sarti, P. Tan, A. Sadhanala, G.-S. Park, Y.-W. Kim, B. Hu, H. J. Bolink, S. Yoo, R. H. Friend, A. M. Rappe, T.-W. Lee, *Nat. Photonics* **2021**, *15*, 148.

[4] H. Shi, Q. Zhang, P. Shi, X. Zhang, *Appl. Phys. Lett.* **2020**, *117*, 261903.

[5] L. Polavarapu, B. Nickel, J. Feldmann, A. S. Urban, *Adv. Energy Mater.* **2017**, *7*, 1700267.

[6] Y. Liu, S. Tang, J. Fan, E. Gracia-Espino, J. Yang, X. Liu, S. Kera, M. Fahlman, C. Larsen, T. Wågberg, L. Edman, J. Wang, *ACS Appl. Nano Mater.* **2021**, *4*, 1162.

[7] J. Li, R. Munir, Y. Fan, T. Niu, Y. Liu, Y. Zhong, Z. Yang, Y. Tian, B. Liu, J. Sun, D.-M. Smilgies, S. Thoroddsen, A. Amassian, K. Zhao, S. Liu, *Joule* **2018**, *2*, 1313.

[8] Q. Hu, L. Zhao, J. Wu, K. Gao, D. Luo, Y. Jiang, Z. Zhang, C. Zhu, E. Schaible, A. Hexemer, C. Wang, Y. Liu, W. Zhang, M. Gratzel, F. Liu, T. P. Russell, R. Zhu, Q. Gong, *Nat. Commun.* **2017**, *8*, 15688.

[9] J. Cao, X. Jing, J. Yan, C. Hu, R. Chen, J. Yin, J. Li, N. Zheng, *J. Am. Chem. Soc.* **2016**, *138*, 9919.

[10] Y. Rong, Z. Tang, Y. Zhao, X. Zhong, S. Venkatesan, H. Graham, M. Patton, Y. Jing, A. M. Guloy, Y. Yao, *Nanoscale* **2015**, *7*, 10595.

[11] M. Liu, N. Yazdani, M. Yarema, M. Jansen, V. Wood, E. H. Sargent, *Nat. Electron.* **2021**, *4*, 548.

[12] Q. A. Akkerman, L. Martínez-Sarti, L. Goldoni, M. Imran, D. Baranov, H. J. Bolink, F. Palazon, L. Manna, *Chem. Mater.* **2018**, *30*, 6915.

[13] J. A. Vigil, A. Hazarika, J. M. Luther, M. F. Toney, *ACS Energy Lett.* **2020**, *5*, 2475.

[14] Q. A. Akkerman, V. D'Innocenzo, S. Accornero, A. Scarpellini, A. Petrozza, M. Prato, L. Manna, *J. Am. Chem. Soc.* **2015**, *137*, 10276.

[15] J. S. Shaikh, N. S. Shaikh, S. S. Mali, J. V. Patil, S. A. Beknalkar, A. P. Patil, N. L. Tarwal, P. Kanjanaboos, C. K. Hong, P. S. Patil, *ChemSusChem* **2019**, *12*, 4724.

[16] J. A. Sichert, Y. Tong, N. Mutz, M. Vollmer, S. Fischer, K. Z. Milowska, R. Garcia Cortadella, B. Nickel, C. Cardenas-Daw, J. K. Stolarczyk, A. S. Urban, J. Feldmann, *Nano Lett.* **2015**, *15*, 6521.

[17] Q. A. Akkerman, T. P. T. Nguyen, S. C. Boehme, F. Montanarella, D. N. Dirin, P. Wechsler, F. Beiglböck, G. Rainò, R. Erni, C. Katan, J. Even, M. V. Kovalenko, *Science* **2022**, *377*, 1406.

[18] N. Fiuza-Maneiro, K. Sun, I. López-Fernández, S. Gómez-Graña, P. Müller-Buschbaum, L. Polavarapu, *ACS Energy Lett.* **2023**, *8*, 1152.

[19] L. M. Wheeler, E. M. Sanehira, A. R. Marshall, P. Schulz, N. C. Anderson, J. A. Christians, D. Nordlund, D. Sokaras, T. Kroll, S. P. Harvey, J. J. Berry, L. Y. Lin, J. M. Luther, *J. Am. Chem. Soc.* **2018**, *140*, 10504.

[20] K. Chen, Q. Zhong, W. Chen, B. Sang, Y. Wang, T. Yang, Y. Liu, Y. Zhang, H. Zhang, *Adv. Funct. Mater.* **2019**, *29*, 1900991.

[21] S. You, H. Zeng, Y. Liu, B. Han, M. Li, L. Li, X. Zheng, R. Guo, L. Luo, Z. Li, C. Zhang, R. Liu, Y. Zhao, S. Zhang, Q. Peng, T. Wang, Q. Chen, F. T. Eickemeyer, B. Carlsen, S. M. Zakeeruddin, L. Mai, Y. Rong, M. Grätzel, X. Li1, *Science* **2023**, *379*, 288.

**ADVANCED
SCIENCE NEWS**

www.advancedsciencenews.com

**ADVANCED
OPTICAL
MATERIALS**

www.advopticalmat.de

[22] M. A. Green, E. D. Dunlop, J. Hohl-Ebinger, M. Yoshita, N. Kopidakis, K. Bothe, D. Hinken, M. Rauer, X. Hao, *Prog. Photovoltaics* **2022**, *30*, 687.

[23] N.-G. Park, *ACS Energy Lett.* **2019**, *4*, 2983.

[24] Y. Qian, Y. Shi, G. Shi, G. Shi, X. Zhang, L. Yuan, Q. Zhong, Y. Liu, Y. Wang, X. Ling, F. Li, M. Cao, S. Li, Q. Zhang, Z. Liu, W. Ma, *Sol. RRL* **2021**, *5*, 2100090.

[25] Q. A. Akkerman, M. Gandini, F. Di Stasio, P. Rastogi, F. Palazon, G. Bertoni, J. M. Ball, M. Prato, A. Petrozza, L. Manna, *Nat. Energy* **2016**, *2*, 16194.

[26] D. Beynon, E. Parvazian, K. Hooper, J. McGettrick, R. Patidar, T. Dunlop, Z. Wei, P. Davies, R. Garcia-Rodriguez, M. Carnie, M. Davies, T. Watson, *Adv. Mater.* **2023**, *35*, 2208561.

[27] A. R. Kirmani, M. Woodhouse, J. M. Luther, *ACS Energy Lett.* **2022**, *7*, 1255.

[28] J. Yuan, C. Bi, S. Wang, R. Guo, T. Shen, L. Zhang, J. Tian, *Adv. Funct. Mater.* **2019**, *29*, 1906615.

[29] L. Qiu, S. He, L. K. Ono, S. Liu, Y. Qi, *ACS Energy Lett.* **2019**, *4*, 2147.

[30] Q. Zhao, R. Han, A. R. Marshall, S. Wang, B. M. Wieliczka, J. Ni, J. Zhang, J. Yuan, J. M. Luther, A. Hazarika, G. R. Li, *Adv. Mater.* **2022**, *34*, 2107888.

[31] M. A. Reus, L. K. Reb, A. F. Weinzierl, C. L. Weindl, R. Guo, T. Xiao, M. Schwartzkopf, A. Chumakov, S. V. Roth, P. Müller-Buschbaum, *Adv. Opt. Mater.* **2022**, *10*, 2102722.

[32] M. Hao, Y. Bai, S. Zeiske, L. Ren, J. Liu, Y. Yuan, N. Zarrabi, N. Cheng, M. Ghasemi, P. Chen, M. Lyu, D. He, J.-H. Yun, Y. Du, Y. Wang, S. Ding, A. Armin, P. Meredith, G. Liu, H.-M. Cheng, L. Wang, *Nat. Energy* **2020**, *5*, 79.

[33] X. Ling, S. Zhou, J. Yuan, J. Shi, Y. Qian, B. W. Larson, Q. Zhao, C. Qin, F. Li, G. Shi, C. Stewart, J. Hu, X. Zhang, J. M. Luther, S. Duhm, W. Ma, *Adv. Energy Mater.* **2019**, *9*, 1900721.

[34] F. Li, S. Zhou, J. Yuan, C. Qin, Y. Yang, J. Shi, X. Ling, Y. Li, W. Ma, *ACS Energy Lett.* **2019**, *4*, 2571.

[35] NREL, Best Research-Cell Efficiency Chart, https://www.nrel.gov/pv/cell-efficiency.html (accessed: April 2023).

[36] R. Sorrentino, M. Gandini, J. M. Figueroa Tapia, A. Petrozza, *Sustainable Energy Fuels* **2020**, *4*, 171.

[37] N. Samantaray, B. Parida, T. Soga, A. Sharma, A. Kapoor, A. Najar, A. Singh, *Phys. Status Solidi A* **2022**, *219*, 2100629.

[38] Y.-F. Ma, Y.-M. Wang, J. Wen, A. Li, X.-L. Li, M. Leng, Y.-B. Zhao, Z.-H. Lu, *J. Electron. Sci. Technol.* **2023**, *21*, 100189.

[39] H. Lee, H.-J. Song, M. Shim, C. Lee, *Energy Environ. Sci.* **2020**, *13*, 404.

[40] A. R. Kirmani, A. D. Sheikh, M. R. Niazi, M. A. Haque, M. Liu, F. P. G. de Arquer, J. Xu, B. Sun, O. Voznyy, N. Gasparini, D. Baran, T. Wu, E. H. Sargent, A. Amassian, *Adv. Mater.* **2018**, *30*, 1801661.

[41] C. Ma, M. Grätzel, N.-G. Park, *ACS Energy Lett.* **2022**, *7*, 3120.

[42] C. Ma, F. T. Eickemeyer, S.-H. Lee, D.-H. Kang, S. J. Kwon, M. Grätzel, N.-G. Park, *Science* **2023**, *379*, 173.

[43] Y. Zou, S. Yuan, A. Buyruk, J. Eichhorn, S. Yin, M. A. Reus, T. Xiao, S. Pratap, S. Liang, C. L. Weindl, W. Chen, C. Mu, I. D. Sharp, T. Ameri, M. Schwartzkopf, S. V. Roth, P. Muller-Buschbaum, *ACS Appl. Mater. Interfaces* **2022**, *14*, 2958.

[44] S. A. McDonald, G. Konstantatos, S. Zhang, P. W. Cyr, E. J. Klem, L. Levina, E. H. Sargent, *Nat. Mater.* **2005**, *4*, 138.

[45] L. Protesescu, S. Yakunin, M. I. Bodnarchuk, F. Krieg, R. Caputo, C. H. Hendon, R. X. Yang, A. Walsh, M. V. Kovalenko, *Nano Lett.* **2015**, *15*, 3692.

[46] B. Dou, J. B. Whitaker, K. Bruening, D. T. Moore, L. M. Wheeler, J. Ryter, N. J. Breslin, J. J. Berry, S. M. Garner, F. S. Barnes, S. E. Shaheen, C. J. Tassone, K. Zhu, M. F. A. M. van Hest, *ACS Energy Lett.* **2018**, *3*, 2558.

[47] B. Parida, A. Singh, A. K. Kalathil Soopy, S. Sangaraju, M. Sundaray, S. Mishra, S. F. Liu, A. Najar, *Adv. Sci.* **2022**, *9*, 2200308.

[48] X. Gu, L. Shaw, K. Gu, M. F. Toney, Z. Bao, *Nat. Commun.* **2018**, *9*, 534.

[49] K. Momma, F. Izumi, *J. Appl. Crystallogr.* **2011**, *44*, 1272.

[50] X. F. Liu, L. Zou, C. Yang, W. Zhao, X. Y. Li, B. Sun, C. X. Hu, Y. Yu, Q. Wang, Q. Zhao, H. L. Zhang, *ACS Appl. Mater. Interfaces* **2020**, *12*, 43073.

[51] H. Huang, J. Raith, S. V. Kershaw, S. Kalytchuk, O. Tomanec, L. Jing, A. S. Susha, R. Zboril, A. L. Rogach, *Nat. Commun.* **2017**, *8*, 996.

[52] W. Chen, J. Zhong, J. Li, N. Saxena, L. P. Kreuzer, H. Liu, L. Song, B. Su, D. Yang, K. Wang, J. Schlipf, V. Korstgens, T. He, K. Wang, P. Müller-Buschbaum, *J. Phys. Chem. Lett.* **2019**, *10*, 2058.

[53] P. Ziherl, R. D. Kamien, *J. Phys. Chem. B* **2001**, *105*, 10147.

[54] S. Shao, M. A. Loi, *Adv. Mater. Interfaces* **2019**, *7*, 1901469.

[55] P. M. Hangoma, I. Shin, H. S. Yang, D. Kim, Y. K. Jung, B. R. Lee, J. H. Kim, K. H. Kim, S. H. Park, *Adv. Funct. Mater.* **2020**, *30*, 2003081.

[56] J. Qi, H. Xiong, G. Wang, H. Xie, W. Jia, Q. Zhang, Y. Li, H. Wang, *J. Power Sources* **2018**, *376*, 46.

[57] W. Chen, H. Tang, N. Li, M. A. Scheel, Y. Xie, D. Li, V. Korstgens, M. Schwartzkopf, S. V. Roth, K. Wang, X. W. Sun, P. Müller-Buschbaum, *Nanoscale Horiz.* **2020**, *5*, 880.

[58] M. A. Reus, L. K. Reb, P. Müller-Buschbaum, INSIGHT: The in situ GIXS heuristic tool for efficient reduction of grazing-incidence scattering data, https://www.ph.nat.tum.de/functmat/forschung/insight/ (accessed: April 2023).

[59] A. Hexemer, P. Muller-Buschbaum, *IUCrJ* **2015**, *2*, 106.

[60] A. L. Oechsle, J. E. Heger, N. Li, S. Yin, S. Bernstorff, P. Muller-Buschbaum, *ACS Appl. Mater. Interfaces* **2022**, *14*, 30802.

[61] R. Kroon, D. A. Mengistie, D. Kiefer, J. Hynynen, J. D. Ryan, L. Yu, C. Muller, *Chem. Soc. Rev.* **2016**, *45*, 6147.

[62] G. Renaud, R. Lazzari, F. Leroy, *Surf. Sci. Rep.* **2009**, *64*, 255.

[63] A. L. Stancik, E. B. Brauns, *Vib. Spectrosc.* **2008**, *47*, 66.

[64] F. Staub, H. Hempel, J.-C. Hebig, J. Mock, U. W. Paetzold, U. Rau, T. Unold, T. Kirchartz, *Phys. Rev. Appl.* **2016**, *6*, 044017.